Numerical Weather Prediction

Fibonacci Grids: a novel approach to Global Modelling

Forecasting Research Technical Report No. 468

Richard Swinbank (Met Office) and R.James Purser (NCEP and SAIC)

email: nwp_publications@metoffice.gov.uk

Document review history

Fibonacci Grids: a novel approach to Global Modeling
File names: Fibonacci_paper_v?.doc (main text)
Fibonacci_appendix_v?.doc (appendices)
Fibonacci_combined_v?.doc (main text and appendices)
Fibonacci_figures_v?.doc (figures)
Authors: Richard Swinbank and Jim Purser

Date	Version	Action/comments:	Approval
1999	1	First draft, written while at DAO	R. Swinbank
09/02/05	2	Minor updates, added references, appendices revised	
26/3/05	3	Notes added to main text (v3) while RS visited RJP Minor changes to appendices (v2) updated, equations revised	
7/4/05		New file incorporating figures and captions (Fibonacci_figures_v1.doc)	
8/4/05	4	Text revised to incorporate points from notes in v3. All 3 files updated to v4 (minor changes to appendices, revised version of some figures)..	
10/5/05	5	Minor changes (main text file only)	
6/12/05	6	Changes for a) Dave Parrish's review b) add Voronoi mesh. Approved for issue as FRTN and submission to QJRMS	Stuart Bell

Fibonacci Grids: a novel approach to Global Modelling

Richard Swinbank, Met Office, Exeter, U.K.

R. James Purser[1], National Centers for Environmental Prediction, Camp Springs, Maryland, U.S.A.

Summary

Recent years have seen a resurgence of interest in a variety of non-standard computational grids for global numerical prediction. The motivation has been to reduce problems associated with the converging meridians and the polar singularities of conventional regular latitude-longitude grids. A further impetus has come from the adoption of massively parallel computers, for which it is necessary to distribute work equitably across the processors; this is more practicable for some non-standard grids. Desirable attributes of a grid for high-order spatial finite differencing are: (i) geometrical regularity; (ii) a homogeneous and approximately isotropic spatial resolution; (iii) a low proportion of the grid points where the numerical procedures require special customization (such as near coordinate singularities or grid edges); (iv) ease of parallelization.

One family of grid arrangements which, to our knowledge, has never before been applied to numerical weather prediction, but which appears to offer several technical advantages, are what we shall refer to as "Fibonacci grids". These grids possess virtually uniform and highly isotropic resolution, with an equal area for each grid point. There are only two compact singular regions on a sphere that require customized numerics. We demonstrate the practicality of this type of grid in shallow water simulations, and discuss the prospects for efficiently using these frameworks in three-dimensional weather prediction or climate models.

KEYWORDS: Global grids Atmospheric modelling

[1] Additional Affiliation: Science Applications International Corporation, Beltsville, Maryland.

1. Introduction

Global grid point atmospheric models generally use a standard framework, in which locally quadrilateral grids are aligned with the latitude and longitude coordinate system. While this approach is superficially simple, it suffers from some fundamental problems that are associated with converging meridians at high latitudes, and singularities at the poles. Recent years have seen a resurgence of interest in a variety of non-standard computational grids for global numerical prediction, to alleviate these problems. A further impetus has come from the adoption of massively parallel computers, for which it is necessary to distribute work equitably across the processors; this is more practicable for some non-standard grids. Desirable attributes of a grid for high-order spatial finite differencing are: (i) geometrical regularity; (ii) a homogeneous and approximately isotropic spatial resolution; (iii) a low proportion of the grid points where the numerical procedures require special customization (such as near coordinate singularities or grid edges); (iv) ease of parallelization.

Two early attempts to alleviate the difficulties of the standard latitude-longitude grid framework are the "skipped grid" introduced by *Gates and Riegel* [1962] and the "reduced grid" proposed by *Kurihara* [1965]. Such solutions preserve approximately constant spatial resolution at all latitudes, but at the additional computational cost and inconvenience associated with the zonal interpolations required to "fill the gaps" pole-ward of each of the latitudes where the grid's zonal resolution is made to change.

An alternative approach is to map the globe onto the faces of an appropriate polyhedron, the faces of which are subdivided to make up the grid cells. *Purser* [1999] has reviewed a range of alternative polyhedral grid frameworks that have been used for global numerical modeling. One example is the use of grid frameworks based on a cube [e.g. *Sadourny*, 1972, *Rančić et al.*, 1996 and *Ronchi et al.*, 1996]. A more popular approach is the use of grid frameworks based on a regular icosahedron [e.g. *Sadourny et al.*, 1968, *Williamson*, 1968, *Cullen*, 1974, *Thuburn*, 1997 and *Majewski et al.*, 2002]. Generally speaking, the polyhedral grids reduce both the problem of converging meridians, and the severity of the "polar" singularities (at the cost of introducing a greater number of locations where customized numerics are required, at the vertices of the underlying polyhedron). In cases where the grids lack smooth continuity across the edges of the polyhedron, special numerical treatment is also required at those locations.

Overset grids, such as the "Yin-Yang" Grid [*Kageyama and Sato* 2004, *Takahashi et al.*, 2005], have also been proposed for global modeling. Such arrangements, in which the globe is covered by two (or more) overlapping grids, preserve grid regularity, avoid singularities, and achieve fairly uniform resolution. However, interpolations have to be done at least once every timestep in the overlap regions.

One family of grid arrangements which, to our knowledge, has never before been applied to numerical weather prediction, but which appears to offer several technical advantages, are what we shall refer to as "Fibonacci grids". They can be thought of as mathematically ideal generalizations of the patterns occurring naturally in the spiral arrangements of seeds and fruit found in sunflower heads and pineapples

(to give two of the many botanical examples). These grids possess virtually uniform and highly isotropic resolution. There are only two compact singular regions on a sphere that require customized numerics.

Saff and Kuijlaars [1997] give a very readable review of general approaches to the problem of distributing many points evenly over the surface of a sphere. They describe approaches which correspond to the "reduced grid" and the icosahedral grid already mentioned. Their construction of a "generalized spiral set" of points is somewhat similar to our spherical Fibonacci Grid, although they do not identify the benefits of using a generation angle based on the golden ratio, which we outline below. The Fibonacci grids are also superficially similar to the spherical spiral grids proposed by *Chukkapalli et al.* [1999], and share some of the same computational advantages. However, the algorithm which defines the Fibonacci grid framework is simpler, and produces a more even distribution of grid-points. The Fibonacci grid combines uniform resolution with a lack of artificial symmetries. More recently, *Hannay and Nye* [2004] proposed the use of a Fibonacci lattice that is essentially identical to our grid, for elementary numerical integration on a sphere.

This paper extends the preliminary work of *Swinbank & Purser*, [1999]. In this paper we describe the Fibonacci grid frameworks, first in 2 dimensions, and later for the surface of a sphere. We describe the implementation of a shallow water model using the spherical Fibonacci grid, and show results produced using that model. Lastly, we discuss the prospects for efficiently using this approach for three-dimensional numerical weather prediction or climate models. Although we anticipate that Fibonacci grid models should be relatively straightforward to implement on massively parallel computers, we do not address that issue directly in the current paper; instead the reader is referred to the paper by *Michalakes et al.* [1999].

2. The Fibonacci Grids

Perhaps the greatest European mathematician of the Middle Ages was Leonardo of Pisa, better known as Fibonacci. While he was largely responsible for the introduction of the Hindu-Arabic notation system for numbers, he is probably better known as the inventor of the Fibonacci sequence of numbers. In the Fibonacci sequence (0, 1, 1, 2, 3, 5, 8, 13,…) each number is the sum of the two numbers that precede it. For many years, it has been realized that patterns seen in many plants and flowers can be characterized by Fibonacci numbers; see, for example, the recent reviews by *Conway and Guy* [1996] and *Stewart* [1998]. Perhaps the most well-known botanical example of such a pattern is the arrangement of the seeds in a sunflower head. The most conspicuous features of this pattern are the successive families of spiral arcs, alternating between right-handed (clockwise) and left-handed (anti-clockwise) curvature. In general the number of spirals in, say, a clockwise family is a Fibonacci number F_k, while the number of anti-clockwise spirals is an adjacent number in the sequence (F_{k+1} or F_{k-1}). (By convention, we index the Fibonacci sequence such that $F_0 = 0$.) As the distance from the centre increases, the spacing of points along a particular spiral first decreases to a minimum, then it starts to increase. The spirals which are most obvious to the eye at any particular radius are those along which the spacing between the points is least; we refer to them as the "dominant" set of spirals. As the radius increases, the order (k) of the dominant spirals also increases.

Bravais and Bravais [1837] were the first to show that such patterns resulted from elements on a unique tightly wound spiral, known as the generative spiral. Measurements on plants showed that the angular spacing between successive elements on the generative spiral are close to 137.5°, or $2\pi(1-\Phi^{-1})$, where Φ is the golden ratio $(1+\sqrt{5})/2$, defined by the relationship $\Phi = 1 + \Phi^{-1}$. *Douady and Couder* [1992] showed that this special angular separation can arise automatically from a system's tendency to avoid periodic organization; each new element fits into the largest gap between the previous set of elements, leading to an even distribution of points over all possible angles. In order to obtain an even distribution of the elements over a disk, *Vogel* [1979] pointed out that the radius of the generative spiral must be proportional to the square root of the angle along the spiral; this type of spiral is sometimes referred to as a Fermat (or cyclotron) spiral. Thus, a mathematical idealization of the "sunflower" pattern can be generated using a simple pair of formulae for the polar radial and azimuthal coordinates r and λ of each point i:

$$\lambda_i = 2\pi i\Phi^{-1}, \tag{1}$$

$$r_i = r_0\sqrt{i-1/2}\,. \tag{2}$$

The angular displacement between successive points is $2\pi\Phi^{-1}$, (or about 222.5° = 360° - 137.5°; Eq. 1). The radial distribution (Eq. 2) ensures that there is one point in each ring of area πr_0^2 centred on the origin, so that the points are evenly spaced in 2 dimensions. The offset of '1/2' in Eq. (2) leads to the most uniform distribution of points in the immediate vicinity of the pole.

We use these formulae to define a planar "Fibonacci Grid"; see Figure 1. This planar Fibonacci grid is a simple way of covering a disk with a virtually uniform set of points. While more efficient arrangements may be attainable for a particular number of points, these formulae are valid for an arbitrary number of points (i.e. an arbitrary range of the index i).

The spherical Fibonacci grid (Figure 2) is obtained by wrapping the planar grid around a sphere in such way as to preserve the equal-area property. The points are arranged at different longitudes λ, in a similar manner to Eq.1. In order to obtain an equal-area grid on the sphere, the points are spaced evenly in $\sin\theta$, where θ is latitude (i.e. every point is at a different latitude). By convention, we index points from $-N$ to $+N$, so that the point indexed 0 is at 0°N, 0°E

$$\lambda_i = 2\pi i\Phi^{-1}, \tag{3}$$

$$\sin\theta = {}^{2i}\!/_{2N+1}. \tag{4}$$

Once again, the polar-most points (i=-N and +N) are offset from the poles: the points are placed in the centre of bands of equal width in $\sin\theta$ that cover the whole globe. By contrast, *Hannay and Nye* [2004] omit this offset and therefore have the pole as the first point of their grid. Whether the equator belongs to, or is staggered with respect to, the sequence of grid points is an arbitrary choice; our choice here to include the equator is made merely for indexing convenience.

For convenience, one can consider the Fibonacci grid points arranged on a cartesian coordinates, with the x-coordinate representing λ and the y-coordinate $\sin\theta$, as shown in Fig. 3; this corresponds to a Lambert equal-area cylindrical projection of the globe [e.g., *Pearson*, 1990]). We can define a set of basis vectors $\mathbf{b}_k$, which are unit vectors corresponding to grid intervals along the spirals (or along the diagonal rows on the cartesian coordinates). The basis vectors $\mathbf{b}_k$ correspond to the displacement between two points whose indices differ by F_k. It follows that the basis vectors obey a similar recurrence relationship to the Fibonacci numbers themselves:

$$\mathbf{b}_{k+1} = \mathbf{b}_k + \mathbf{b}_{k-1}. \tag{5}$$

From Figure 3, it is clear that the components of the basis vectors can be written in terms of the "circumference" in λ ($C=2\pi$), and the y-interval ($\delta=A/2\pi$, where A is the area per grid-point):

$$\mathbf{b}_k = \left\{ (-)^k \, 2\pi\Phi^{-k}, F_k \, A/2\pi \right\}. \tag{6}$$

Equation (6) may be rewritten to give the basis vectors in terms of local cartesian coordinates on the surface of the unit sphere (recalling that $A=4\pi/(2N+1)$):

$$\mathbf{b}_k = \left\{ (-)^k \, 2\pi\cos\theta\Phi^{-k}, \frac{2F_k}{(2N+1)\cos\theta} \right\}. \tag{7}$$

One can apply a similar technique to determine the basis vectors for the planar "sunflower" grid. In that case the vertical axis of Figure 3 corresponds to the square of the radial coordinate r and the horizontal axis corresponds to the azimuthal coordinate λ. It follows that the basis vectors on the planar grid are given by:

$$\mathbf{b}_k = \left\{ (-)^k \, 2\pi r\Phi^{-k}, \frac{F_k r_0^2}{2r} \right\}. \tag{8}$$

On the spherical grid, as on the planar grid, different spirals dominate at different latitudes. Using the relationship $F_k \approx \Phi^k/\sqrt{5}$ when $k \gg 1$, to a good approximation, $\mathbf{b}_k$ can be written in the form

$$\mathbf{b}_k = d\left\{ (-)^k \, \Phi^{z-k}, \Phi^{k-z} \right\}, \tag{9}$$

where the "zone number" z is defined by

$$\Phi^{2z} = (2N+1)\pi\sqrt{5}\cos^2\theta \tag{10}$$

and the length scale d is given by

$$d^2 = \frac{4\pi}{\sqrt{5}(2N+1)} = \frac{A}{\sqrt{5}}. \tag{11}$$

The zone number is equal to k at the latitude at which $|\mathbf{b}_k|$ is minimum; here the dominant spiral is of order k and the minimum grid-length, along that spiral, is $\sqrt{2}.d$. The next most dominant spirals (k-1 and k+1) each have grid lengths $\sqrt{3}.d$. Where the zone number is k+½, spirals k and k+1 are equally dominant and the points form a square grid, of grid-length $5^{\frac{1}{4}}d$, or $\sqrt{A}$. (For the planar sunflower grid, Eq. 9 also holds, and equivalent expressions to Eqs 10 and 11 may be derived for z and d.)

In order to identify the nearest neighbours of every grid point, we perform a Delaunay triangulation on the points of the spherical Fibonacci grid. As discussed in [e.g.] *Chynoweth and Sewell* [1990], a Delaunay triangulation can be constructed from an arbitrary set of points by joining the points to form a set of triangles, such that, if a circle is drawn through the vertices of each triangle, there are no other points within that circle. Figure 4a shows the Delaunay triangulation for the points illustrated in Figure 2. The triangulation highlights the zone structure of the Fibonacci grid; at zone numbers of the form k+1/2 (where the grid is square), there is a transition from one set of approximately 45° isosceles triangles to a set oriented in the opposite sense. A Voronoi mesh (e.g., *Augenbaum and Peskin*, [1985]) is the dual of the Delaunay triangulation, and delineates cells centred on the grid points. Figure 4b shows the Voronoi mesh for the same grid as Figs 4a and 2. In most cases, each grid-point has 6 neighbours (defined as the other points linked to it by the edges of the triangles), so the Voronoi cells are irregular hexagons. However, in some cases there are 5 or 7 neighbouring points, leading to pentagonal and heptagonal cells.

In each case the Delaunay triangles are formed by a triple of basis vectors $\mathbf{b}_{k-1}$, $\mathbf{b}_k$ and $\mathbf{b}_{k+1}$. On the equal area cylindrical projection, it is simple to show that each of these small triangles has exactly the same area (= A/2). However, on the surface of the sphere, the areas are not identical, because the edges of the spherical triangles are formed by great circles, rather than the straight lines from the cylindrical equal area projection. To illustrate the equal-area nature of the Fibonacci grid, it is best to consider the areas of the Voronoi cells, since they can be considered to be the areas represented by each grid point. Figure 5 shows histograms of the areas of the Voronoi cells for three different resolutions of the Fibonacci grid. The cells with areas most different from the average occur close to the poles. As the grid resolution is improved (N is increased), areas of the cells away from the poles become closer and closer to the average and the absolute number of cells with areas different from average hardly changes. In this sense, the Fibonacci Grid is a very close approximation to an equal-area grid.

Finally, we note that there are a number of variations of the basic Fibonacci grid. First, the grid exists in two chiral forms (i.e., right- and left-hand forms), obtained by changing the sign of the angular increment in Eq. 3). Secondly, a degree of rotational symmetry can be introduced by having several points spaced evenly around each latitude circle. Thirdly, the latitudinal spacing can be varied, while retaining the quasi-isotropic properties of the grid. This framework might be useful for a global ocean model, in which resolution is increased in the tropics (Fig. 6).

3. Shallow water model

The spherical Fibonacci grid has several attributes that make it suitable for numerical modelling, notably its geometric regularity, its almost homogeneous and

isotropic resolution, and lack of artificial symmetries. A major advantage over the usual regular latitude-longitude grid is that it does not suffer from converging meridians, for which the resulting small grid-lengths near the poles necessitate the use of techniques such as Fourier filtering to remove small-scale instabilities. The extra resolution near the poles also means that a disproportionate amount of work needs to be spent on physical parametrizations at high latitudes. The strong inhomogeneity in grid sizes may itself lead to difficulties in determining the degree to which sub grid-scale effects need to be parametrized. The advantages of the Fibonacci grid are achieved without the introduction of the multiplicity of singular points which occur when using polyhedral grid frameworks. However, computations on the Fibonacci grid still require special numerical treatment of the polar caps.

In order to demonstrate the feasibility of using the Fibonacci grid for global numerical modelling, we have written a model to solve the Eulerian shallow water equations on that grid. One disadvantage of the Fibonacci grid is that there is not a natural way to stagger the grid points. However, by using the combination of high order differencing with low-pass filtering to combat the tendency towards nonlinear computational instability, we anticipate that we can overcome the inherent disadvantages of an unstaggered grid.

Over most of the globe, we solve the shallow water equations written in terms of the equal-area cylindrical mapping; in this mapping, the "spirals" are straight lines, as shown in Figure 3. In the neighbourhood of the poles, where the spirals lose their identity, we use a set of equations written using the azimuthal equal area mapping; this is equivalent to using the planar grid illustrated in Fig. 1. Appendix A shows how the shallow water equations can be written in both equal-area coordinate systems.

For the equal-area cylindrical projection, Eqs (A14) and (A18) can be expanded to give equations for the contravariant westerly and southerly wind components ($\dot{x}$ and $\dot{y}$) and the height *h*:

$$\frac{\partial \dot{x}}{\partial t} = -\dot{x}\frac{\partial \dot{x}}{\partial x} - \dot{y}\frac{\partial \dot{x}}{\partial y} + \frac{2\sin\theta}{\cos^2\theta}\dot{x}\dot{y} + \frac{1}{\cos^2\theta} f\,\dot{y} - \frac{g}{\cos^2\theta}\frac{\partial h}{\partial x}, \tag{12}$$

$$\frac{\partial \dot{y}}{\partial t} = -\dot{x}\frac{\partial \dot{y}}{\partial x} - \dot{y}\frac{\partial \dot{y}}{\partial y} - \sin\theta\cos^2\theta\dot{x}^2 - \frac{\sin\theta}{\cos^2\theta}\dot{y}^2 - \cos^2\theta f\,\dot{x} - g\cos^2\theta\frac{\partial h}{\partial y}, \tag{13}$$

$$\frac{\partial h}{\partial t} = -\dot{x}\frac{\partial h}{\partial x} - \dot{y}\frac{\partial h}{\partial y} - h\left\{\frac{\partial \dot{x}}{\partial x} + \frac{\partial \dot{y}}{\partial y}\right\}. \tag{14}$$

For each grid point, high-order derivatives are calculated along each of the three locally dominant basis vectors (i.e., along the dominant spirals). The *x*- and *y*-components of the gradients are calculated by linearly combining those derivatives. The *x*- and *y*- derivatives of a scalar *a* are related to the along-spiral gradients by:

$$\left[\frac{da}{dS_k},\quad \frac{da}{dS_{k+1}}\right]=\left[\frac{\partial a}{\partial x},\quad \frac{\partial a}{\partial y}\right]\begin{bmatrix}\dfrac{dx}{dS_k}, & \dfrac{dx}{dS_{k+1}}\\ \dfrac{dy}{dS_k}, & \dfrac{dy}{dS_{k+1}}\end{bmatrix}, \tag{15}$$

where the components of the basis vector $\mathbf{b}_k$ in the cylindrical coordinate system are denoted by $[dx/dS_k,\ dy/dS_k]$. The matrix in this equation has determinant $(-)^k A$, so this result may be inverted to get:

$$\left[\frac{\partial a}{\partial x},\frac{\partial a}{\partial y}\right]=\frac{(-)^k}{A}\left[\frac{da}{dS_k},\frac{da}{dS_{k+1}}\right]\begin{bmatrix}\dfrac{dy}{dS_{k+1}}, & -\dfrac{dx}{dS_{k+1}}\\ -\dfrac{dy}{dS_k}, & \dfrac{dx}{dS_k}\end{bmatrix} \tag{16}$$

Only one pair of basis vectors (in this case $\mathbf{b}_k$ and $\mathbf{b}_{k+1}$) is strictly necessary for gradient computations. But more smoothly varying gradient calculations can be obtained by combining the high-order derivatives along each of the three locally-dominant basis vectors. At the latitude corresponding to zone number k+½ the gradients are calculated using Eq. (16), and at the latitude corresponding to zone number k-½ a similar expression is used, but based on the pair of basis vectors $\mathbf{b}_{k-1}$ and $\mathbf{b}_k$. For latitudes between zone numbers k+½ and k-½, a linear combination of the two expressions is used, with a weighting that varies smoothly with latitude.

The regular approach described above cannot be applied to the polar caps, where the points are effectively configured amorphously, and we are forced to adopt customized differencing stencils and coefficients to achieve high order accuracy. The schemes are more costly (per target) to apply, but are required only at a small minority of the points of the whole model, so the burden is tolerable. Regardless of the resolution, the polar equal-area mapping of the grid (i.e., from the spherical grid to the planar grid) leads to the same geometrical configuration on the plane, except for a trivial constant scaling and rotation. Thus, the customized differencing coefficients need to be worked out only once for each intended order of accuracy.

The approach we take to compute the stencil coefficients here is the planar analogue of the collocation method discussed by *Swarztrauber et al.* [1997]. It is explained in detail in Appendix B. At point j the x- and y- derivatives of a field a, in polar coordinates, are given by

$$\left(\frac{\partial a}{\partial x}\right)_j=\sum_{i=0}^{n} C_{ij}^{X} a_i, \tag{17}$$

$$\left(\frac{\partial a}{\partial y}\right)_j=\sum_{i=0}^{n} C_{ij}^{Y} a_i, \tag{18}$$

where C^X_{ij} and C^Y_{ij} are stencil coefficients; each stencil comprises the target point (i=0), and n neighbours (the number of neighbours depends on the required order of accuracy of the derivatives).

A similar method, but using low order numerics, provides the unstructured stencil coefficients for the Laplacian operator, which is the basis for constructing low-pass filters. (Those low-pass filters are analogous to the diffusion normally applied in NWP models; for brevity we will often refer to this filtering as "diffusion"). In the results presented here, we apply the Laplacian filter twice, in such a way as to produce ∇^4 filtering. The set of stencil points used for the Laplacian operator at each grid point consists of the point itself together with the neighbouring points from the Delaunay triangulation. The expression for the Laplacian operator is:

$$\left(\nabla^2 a\right)_j = \sum_{i=0}^{n} C_{ij}^L a_i , \tag{19}$$

where C^L_{ij} are the stencil coefficients for neighbour i of point j, and n is the number of neighbours (in the range 5 to 7). Higher order diffusion is obtained by applying the Laplacian operator several times. This method could also be used for the construction of relaxation operators to solve the Helmholtz equations associated with the solution procedures required for possible future semi-implicit versions of this model.

In practice, it was found that a substantial amount of diffusion was required to maintain computational stability. The shallow water model is somewhat more prone to computational instability at high latitudes. This may reflect greater inaccuracies associated with the regular differencing at high latitudes, and perhaps also difficulties with determining tendencies for the amorphously distributed points in the polar cap. Accordingly, we included the facility to vary the diffusive filtering coefficient as a function of latitude. However, for the results presented in this paper, we found it simpler to filter the model fields with the same strength filter over the whole globe.

The shallow-water model at present uses a fourth-order Runge-Kutta time integration scheme (e.g. *Press et al*, [1996], chapter 16). Although it would be possible to use a more efficient time integration scheme, we have focused primarily on spatial aspects in this paper, since we are concerned with a novel spatial grid. The order of accuracy of the spatial derivative calculations may be varied. For the results presented here, the along-spiral derivatives are calculated using 4^{th} order accurate finite differences. 4^{th} order accurate derivatives are also used for the polar parts of the model solution.

4. Results

In order to make an assessment of the model performance, we have carried out some of the standard tests defined by *Williamson et al.* [1992]. First, we have tested the advection scheme of the model in isolation, by advecting a cosine bell pattern with a constant, specified wind field. Second, we have used the full shallow-water model to calculate the evolution of a Rossby-Haurwitz wave. For initial studies, as reported by *Swinbank and Purser* [1999], we used a low resolution with N=1000 [2001 grid points, with a nominal grid-length ($\sqrt{A}$) of approximately 500 km]. For this paper, we present results produced at medium resolution (N=5000, grid-length approximately 225 km) and at high resolution (N=20000, grid-length approximately 112 km). The results presented here are all produced using fourth-order accurate horizontal differencing both for the normal zone-differencing and over the polar caps.

a) Advection tests

In these tests a cosine bell is advected once around the sphere, using a specified wind field that corresponds to sold body rotation. The magnitude of the wind is chosen so that after 12 days the solution should exactly overlay the initial data. Several orientations of the advecting wind are specified: around the equator, directly over the poles and minor shifts from these two orientations. The orientations are specified using a parameter α, which is that angle between the axis of solid body rotation and the polar axis. We have run tests with α=0.0, -0.05, +0.05, $\pi/2$, $\pi/2$-0.05, $\pi/2$+0.05. The values of α which are additional to those specified by *Williamson et al.* (α=-0.05, $\pi/2$+0.05) were included because the chirality of the Fibonacci grid means that those solutions are not just reflections of the solutions for α=+0.05 and α= $\pi/2$-0.05. Plots of the advection results for the six different orientations were found to be essentially indistinguishable, so results are only plotted for the over-the-pole case (α= $\pi/2$).

Figure 7(a) shows the results of advecting the cosine bell over the pole using a grid resolution of N=5000 (grid-length approximately 225 km), with the diffusion set close to the minimum value required for stability. All the model results are plotted by interpolating from the model grid to a one-degree resolution latitude-longitude grid. Since that resolution is finer than the model resolutions we have used, any structures on the model grid-scale will be visible in the plotted maps. The final position of the cosine bell pattern is very close to its initial position, as it should be. The main difference is a slight spreading of the pattern, which results from the numerical diffusion.

However, in order to run the full shallow-water model, it proved necessary to run with rather higher diffusion settings. Figure 7(b) shows the advection tests with diffusion settings as required by the full model. In that case, the diffusion has smoothed out the cosine bell much more strongly, although its position is still in very good agreement with its starting location. Figure 7(c) shows the advection results with N=20000 (112 km), again with diffusion setting used in the full model. In that case the finer grid means that the diffusion is having much less effect, and results are essentially the same as for N=5000, with low diffusion,

Figure 8 shows statistical comparisons of the advection results with the true solution. We plot time series of the mean, root mean square and maximum differences, in terms of the L_1, L_2 and L_∞ diagnostics defined by *Williamson et al*. These statistics are calculated from the output fields on the original model grid, assuming that each grid point represents the same area, i.e. there is no area-weighting in the calculations. Figure 8 shows that L_2 and L_∞ grow quickly from the beginning of the integrations, as one would anticipate from errors dominated by diffusion. The mean differences L_1 highlight when the cosine bell is advected over the pole (at days 3 and 9), showing that the grid is not quite equal-area close to the pole.

In summary, the results show that the advective processes are treated well on the Fibonacci Grid. However, the steep gradients in the cosine bell pattern make it particularly susceptible to the diffusive filtering.

b) Rossby-Haurwitz wave

Another test commonly applied to shallow-water models is the simulation of Rossby-Haurwitz waves. The initial height and velocity fields are defined by analytic functions of latitude, longitude and various wave parameters. In a non-divergent barotropic model the wave pattern moves eastward without changing shape. While the Rossby-Haurwitz waves are not analytic solutions of the shallow-water equations, they evolve in a somewhat similar manner, progressing eastward with some change of shape.

Simulations of the Rossby-Haurwitz wave have been performed using both 2^{nd} order and 4^{th} order accurate spatial differencing. Experiments showed that the 2^{nd} order accurate version of the model was more numerically stable than the 4^{th} order version. However, the 4^{th} order solutions were more realistic, and we only show those results in this paper. As noted in the previous section, it was found that it was necessary to increase the diffusion from the levels necessary for the advection tests.

The Rossby-Hauwitz wave tests have been run at both medium (N=5000) and high (N=20000) resolution, each for a 14-day period. Figure 9 shows the starting conditions (day 0) and results at day 14 from the two Fibonacci shallow-water model runs, along with the day 14 reference solution from *Williamson et al.* [1992]. It is worth noting that, for this test, the true solution is not known, and the reference solution is obtained from an independent high resolution model. The medium-resolution results (Fig 9c) are essentially in phase with the reference solution (Fig 9b), but the shape of the waves has changed significantly. The troughs have become more intense and the ridges have become narrower, coupled with an increase in heights at high latitudes. The waves have acquired a noticeable poleward-westward tilt. This tilt is evidence of vacillations in wave structure that have also been found in solutions from other numerical models (see *Thuburn and Li*, [2000]). There is a degree of asymmetry between the solutions in the two hemispheres that results from the chirality of the model grid. There are other small asymmetries between individual waves within a hemisphere, which result from the asymmetric nature of the grid. At high resolution (N=20000, Fig 9d), the overall shape of the wave is closer to the reference solution, and the initial conditions, indicating the improved accuracy resulting from better resolution.

Figure 10 quantifies the errors from the two model runs. In this case, the errors grow relatively slowly at the start, as the solutions gradually diverge. This indicates that, for this test, the errors are not so dominated by the diffusion. The L_1 error confirms that the total mass is not conserved; while the conservation of total mass is not enforced in the model, the statistics indicate that it is not a major problem. The normalized errors L_2, L_∞ errors are much smaller than in the advection test, and probably more indicative of values obtainable in real-life situations.

5. Discussion

The results shown in section 4 demonstrate that it is feasible to build a shallow-water model using the Fibonacci Grid framework. The experiments show that the Fibonacci Grid framework allows accurate advection results. However, the

high diffusion required to run the Eulerian shallow-water model for the Rossby-Haurwitz wave tests show that the model has limitations.

As noted above, the integration scheme does not enforce the conservation of mass. The initial wind fields for the Rossby-Haurwitz wave test case are exactly non-divergent. However, examination of individual terms in the model equations shows that the calculated divergence is non-zero. The errors in the calculated divergence are largest at high latitudes, where the spirals become more curved, and the gradients calculated from along-spiral differences are less accurate. Inaccuracies in the calculation also vary depending on which set of spirals are used for the gradient calculations. This can introduce small-scale "noise" into the tendencies where the zone number changes rapidly (again, at high latitudes), which is one reason why strong diffusion is required to keep the model integration stable.

Thuburn and Li [2000] have shown that the simulation of Rossby-Haurwitz waves is a problem that is particularly sensitive to numerical instabilities. *Hoskins* [1973] showed that Rossby-Haurwitz waves with wavenumber less than or equal to 5 are stable, but Thuburn and Li showed that the solution of the Rossby-Haurwitz wave in shallow water models involves a cascade of energy to smaller scales. Depending on the details of the model grid, the small scale features may project onto unstable modes of the model. This may be a further reason why strong diffusion is required in the Fibonacci Grid shallow-water model.

Difficulties with the accurate calculation of divergences indicate that it may be difficult to enforce conservation properties in the model equations. We do not, either explicitly or implicitly, have a grid-cell structure which we could use to define fluxes of mass or other quantities. One option might be to base a model on a set of triangular grid cells defined using the Delaunay triangulation of a Fibonacci Grid. That would facilitate the enforcement of conservation in the model, but it would make it much harder to implement high-order accurate numerics. Another option would be to formulate a model using the Voronoi cells. Most of the cells would be irregular hexagons, but with some pentagons and heptagons. While this might allow a more accurate calculation of fluxes and divergence, it may be so much more complex as to be impractical – certainly less practical than the geodesic grid with icosahedral symmetry.

In the polar caps, the divergence is captured better, but the pressure gradient term is more of a problem. The Coriolis term acts at right angles to the wind, and is, to a good approximation, balanced by the pressure gradient term. However, in the polar equal-area projection the angles get distorted away from the pole, and the apparent angle between the pressure gradient and the wind direction can be very different. Small inaccuracies in the calculation in polar coordinates can transform back into larger inaccuracies in the local cartesian coordinates.

6. Conclusions

We have described a novel approach to constructing a global model grid, which we refer to as a "Fibonacci Grid". This approach offers a number of significant advantages over previous model grids, notably its virtually uniform and isotropic resolution. It avoids the converging meridians of the standard latitude-longitude grid,

and the consequent need for Fourier filtering. However, the treatment of the polar caps is rather complex.

This paper has demonstrated the feasibility of using this grid for a high-order accurate Eulerian finite-difference model of the shallow-water equations. However, we have identified some problems with this version of the model, which are made evident through some inaccuracies in the calculation of some of the terms in the model tendencies. In this paper, we have concentrated on spatial rather than temporal issues, since our aim has been to demonstrate the use of the innovative Fibonacci Grid. For this grid to be used for an efficient, accurate and practical numerical weather prediction model, a semi-implicit treatment would be required. This would require a Helmholtz solver to be written for a spherical Fibonacci grid. Another possible area for future work would be to demonstrate the feasibility of using the grid for semi-Lagrangian integration schemes. In addition, a Fibonacci grid could be used as a test-bed for amorphous grid techniques, since it does not impose artificial symmetries on the solutions.

Finally, we remark that, although we have focused on the use of Fibonacci grids for global numerical modelling, we anticipate that they could have a range of other applications. The use of the grid for numerical integration, as proposed by *Hannay and Nye* [2004], is just one example. In this context *Purser and Swinbank* [2006] show that, owing to certain fortuitous geometrical properties of the Fibonacci grids, whether staggered or unstaggered with respect to the poles, both these grids admit arbitrarily high-order global integration formulae whose weights are constant except for a handful of the most northerly and the most southerly grid points. The problem of distributing a large number of points uniformly over the surface of a sphere has not only inspired mathematicians, but also scientists working in many diverse fields. While the set of points generated by the Fibonacci grid algorithm may not be quite optimal, it is a very simple method of generating an "almost uniformly" distributed set of an arbitrary number of points over the surface of a sphere.

Acknowledgements: We thank Steve Thomas, Larry Shumaker and David Pearson for drawing our attention to previous research papers. We thank Andrew Staniforth and John Drake for their helpful comments, Dave Parrish for his review of an early version of the manuscript and Ricky Rood for his encouragement. Part of this work was done while RS was working as a Visiting Fellow at the Data Assimilation Office at NASA Goddard Space Flight Center, where he was employed by Universities Space Research Association on contract NAS5-98181.

Appendix A

Shallow water equations in equal-area coordinates

We adopt tensor notation (e.g. *Synge and Schild* [1978]) and the methods of variational mechanics, which provide succinct derivations of the equations for shallow water dynamics in a variety of coordinate systems based on the stationarity of the action integral,

$$\mathcal{L} = \int_{t_1}^{t_2} L dt \tag{A1}$$

with respect to independent variations of the generalized position and momentum variables. We express Hamilton's principle for the dynamics of shallow water in a rotating frame with equal-area map coordinates $\mathbf{x} \equiv (x^1, x^2)$ and, following *Salmon* [1983, 1985], we shall use τ to denote the Lagrangian time coordinate and $\boldsymbol{\alpha} \equiv (\alpha, \beta)$ to denote a pair of Lagrangian particle coordinate labels such that the depth of the flow has the form

$$h = \frac{\partial(\alpha, \beta)}{\partial(x, y)} \equiv \frac{\partial(\boldsymbol{\alpha})}{\partial(\mathbf{x})}. \tag{A2}$$

To simplify matters, we assume the map coordinates are scaled to give unity for the determinant of the (covariant) metric tensor, q_{ij}. Then the "Levi-Civita" tensor operator that rotates a horizontal vector 90 degrees clockwise (viewed from above) will be denoted **E** and, in right-handed equal area coordinates, has the identical contravariant and covariant representations:

$$E^{ij} \equiv E_{ij} \equiv \begin{bmatrix} 0 & 1 \\ -1 & 0 \end{bmatrix}. \tag{A3}$$

The (scalar) cross product of horizontal vectors **A** and **B** is given in tensor notation by $\mathbf{AxB} = A^i B^j E_{ij}$ while the (scalar) curl of a horizontal vector field **A** is given by $\mathrm{curl}(\mathbf{A}) = \partial(E^{ij} A_j)/\partial x^i$. *Salmon* [1983] shows that the effect of a Coriolis parameter in geophysical fluid motion can be introduced through the use of a vector field whose curl is the local Coriolis parameter. Let A_i henceforth denote the covariant representation of such a field, i.e.,

$$\frac{\partial\left(E^{ij} A_j\right)}{\partial x^i} = f(\mathbf{x}). \tag{A4}$$

With $\dot{x}^i$ used as a shorthand for the Lagrangian partial time derivative, $\partial x^i/\partial\tau$, the Lagrangian, L of (A1) then has the form for shallow water:

$$L = \iint \left(u_i + A_i\right)\dot{x}^i \, d\alpha \, d\beta - H, \tag{A5}$$

where the Hamiltonian, H, is the sum of kinetic and potential energies:

$$H\left(\mathbf{u}(\boldsymbol{\alpha}),\mathbf{x}(\boldsymbol{\alpha})\right)=\frac{1}{2}\iint\left(u_i u_j q^{ij}+gh\right)d\alpha d\beta\,. \tag{A6}$$

We identify conditions of stationarity with respect to variations of u_i and of x^i as follows.

$$\delta u_i:\quad \dot{x}^i-q^{ij}u_j=0\,, \tag{A7}$$

which shows that the quantities u_i conjugate to x^i are indeed the proper momentum variables consistent with the kinematic motion.

$$\delta x^i:\quad -\dot{u}_i+\left(-\frac{\partial A_i}{\partial x^j}+\frac{\partial A_j}{\partial x^i}\right)\dot{x}^j-\frac{1}{2}u_j u_k\frac{\partial q^{jk}}{\partial x^i}-g\frac{\partial h}{\partial x^i}=0\,. \tag{A8}$$

The final term of (A8) comes about because

$$\begin{aligned}\delta\iint-\frac{1}{2}ghd\alpha d\beta&=\delta\iint-\frac{1}{2}g\left(\frac{\partial(\mathbf{x})}{\partial(\boldsymbol{\alpha})}\right)^{-1}d\alpha d\beta\\&=\iint\frac{gh^2}{2}\frac{\partial\delta x^i}{\partial x^i}dx^1dx^2\,.\end{aligned} \tag{A9}$$

Then, integrating by parts, this becomes:

$$\begin{aligned}\delta\iint-\frac{1}{2}gh\,d\alpha d\beta&=\iint-g\frac{\partial h}{\partial x^i}\delta x^i h dx^1dx^2\\&=\iint-g\frac{\partial h}{\partial x^i}\delta x^i\,d\alpha d\beta\,.\end{aligned} \tag{A10}$$

The term of (A8) involving **A** can be simplified:

$$\left(-\frac{\partial A_i}{\partial x^j}+\frac{\partial A_j}{\partial x^i}\right)\dot{x}^j=f_{ij}\dot{x}^j \tag{A11}$$

where, by virtue of (A4), the new "Coriolis tensor" is just $f_{ij}=E_{ij}f$.

It becomes inconvenient to retain both representations u_i and $\dot{x}^i$ of the velocity field, but (A7) allows us to eliminate one of these. Keeping $\dot{x}^i$, we obtain:

$$q_{ij}\ddot{x}^j+\{jk,i\}\dot{x}^j\dot{x}^k-f_{ij}\dot{x}^j+g\frac{\partial h}{\partial x^i}=0\,, \tag{A12}$$

where $\{jk,i\}$ denotes the Christoffel symbol of the first kind:

$$\{jk,i\}=\frac{1}{2}\left(\frac{\partial q_{ij}}{\partial x^k}+\frac{\partial q_{ik}}{\partial x^j}-\frac{\partial q_{jk}}{\partial x^i}\right). \tag{A13}$$

In terms of the local time derivative of $\dot{x}^i$, we therefore obtain:

$$\frac{\partial \dot{x}^i}{\partial t} + \frac{\partial \dot{x}^i}{\partial x^j}\dot{x}^j + \Gamma^i_{jk}\dot{x}^j\dot{x}^k - f^i_j\dot{x}^j + gq^{ij}\frac{\partial h}{\partial x^j} = 0\,, \tag{A14}$$

where

$$\Gamma^i_{jk} = q^{il}\{jk, l\}\,, \tag{A15}$$

is the Christoffel symbol of the second kind and the Coriolis mixed-tensor, $f^i_j = q^{ik}E_{kj}f$.

Applying the identity,

$$\frac{d}{d\tau}\log(\det \mathbf{N}) = trace\left(\mathbf{N}^{-1}\frac{d\mathbf{N}}{d\tau}\right), \tag{A16}$$

to the definition of h^{-1} we obtain:

$$\begin{aligned} -\frac{\partial}{\partial \tau}\log h &= \frac{\partial \alpha}{\partial x^i}\frac{\partial^2 x^i}{\partial \alpha \partial \tau} + \frac{\partial \beta}{\partial x^i}\frac{\partial^2 x^i}{\partial \beta \partial \tau} \\ &= \frac{\partial \dot{x}^i}{\partial x^i}\,, \end{aligned} \tag{A17}$$

or, in terms of the Eulerian time derivative,

$$\frac{\partial h}{\partial t} = -\frac{\partial h}{\partial x^i}\dot{x}^i - h\frac{\partial \dot{x}^i}{\partial x^i}\,. \tag{A18}$$

Two equal area mappings, the polar azimuthal and the cylindrical, are natural frameworks for the expression of dynamics on a Fibonacci grid, so we briefly summarize their metrical properties.

(i) Cylindrical mapping

In this case, the appropriate map coordinates preserving correct areas of the unit sphere are

$$\mathbf{x} \equiv (x, y) = \left(\lambda, \sin\theta\right), \tag{A19}$$

and the metric tensor representations are diagonal with

$$q_{xx} = q^{yy} = 1 - y^2\,, \tag{A20a}$$

$$q_{yy} = q^{xx} = 1\Big/\left(1 - y^2\right). \tag{A20b}$$

The components of Γ^i_{jk} are found to be:

$$\Gamma^x_{xx} = -\Gamma^y_{xy} = 0\,, \tag{A21a}$$

$$\Gamma^y_{yy} = -\Gamma^x_{xy} = y/(1-y^2)\,, \tag{A21b}$$

$$\Gamma^x_{yy} = 0\,, \tag{A21c}$$

$$\Gamma^y_{xx} = y(1-y^2)\,. \tag{A21d}$$

(ii) Polar azimuthal mapping

In order that the centered circle of radius r in the map domain encloses the correct area of the corresponding polar cap of the unit sphere we require:

$$r = 2\sin(\theta_c/2) = \frac{\sin\theta_c}{\cos(\theta_c/2)}\,, \tag{A22}$$

where θ_c is the colatitude for this pole. The local metrical properties are determined by the measure of distortion:

$$m = \frac{\partial r}{\partial \theta_c} = \cos(\theta_c/2)\,, \tag{A23}$$

which, in terms of the map coordinates, is defined by:

$$m^2 = 1 - \frac{r^2}{4}\,. \tag{A24}$$

Adopting cartesian map coordinates,

$$\mathbf{x} \equiv (x,y) \equiv \left(r\cos\lambda, r\sin\lambda\right) \tag{A25}$$

where λ is the azimuth (±longitude) about the pole, and the convenient substitution,

$$T = \frac{1}{4m^2} = \frac{1}{4-r^2}\,, \tag{A26}$$

the components of the representations of the metric tensor are found to be:

$$q_{ij} = \begin{bmatrix} 1-y^2/4+x^2T, & xy/4+xyT \\ xy/4+xyT, & 1-x^2/4+y^2T \end{bmatrix} \tag{A27a}$$

$$q^{ij} = \begin{bmatrix} 1-x^2/4+y^2T, & -xy/4-xyT \\ -xy/4-xyT, & 1-y^2/4+x^2T \end{bmatrix}. \tag{A27b}$$

Then, with outer subscripts denoting partial differentiation in the following set of formulae:

$$(q_{xx})_x = x(2T + 2x^2T^2)\,, \tag{A28a}$$
$$(q_{yx})_x = (q_{xy})_x = y(1/4 + T + 2x^2T^2)\,, \tag{A28b}$$
$$(q_{yy})_x = x(-1/2 + 2y^2T^2)\,, \tag{A28c}$$
$$(q_{xx})_y = y(-1/2 + 2x^2T^2)\,, \tag{A28d}$$
$$(q_{yx})_y = (q_{xy})_y = x(1/4 + T + 2y^2T^2)\,, \tag{A28e}$$
$$(q_{yy})_y = y(2T + 2y^2T^2)\,, \tag{A28f}$$

we may use these to obtain, by (A13), the components of the Christoffel symbol, $\{jk,i\}$:

$$\{xx,x\} = x\left(T + x^2T^2\right), \tag{A29a}$$
$$\{yx,x\} = \{xy,x\} = y\left(-1/4 + x^2T^2\right), \tag{A29b}$$
$$\{yy,x\} = x\left(1/2 + T + y^2T^2\right), \tag{A29c}$$
$$\{xx,y\} = y\left(1/2 + T + x^2T^2\right), \tag{A29d}$$
$$\{yx,y\} = \{xy,y\} = x\left(-1/4 + y^2T^2\right), \tag{A29e}$$
$$\{yy,y\} = y\left(T + y^2T^2\right). \tag{A29f}$$

Hence, by applying (A15) and collecting terms, we get the coefficients of the Christoffel symbol, Γ^i_{jk}:

$$\Gamma^x_{xx} = -\Gamma^y_{xy} = xT\left[1 - y^2\left(10 - r^2\right)/8\right], \tag{A30a}$$
$$\Gamma^y_{yy} = -\Gamma^x_{xy} = yT\left[1 - x^2\left(10 - r^2\right)/8\right], \tag{A30b}$$
$$\Gamma^x_{yy} = xT\left[3 - x^2\left(10 - r^2\right)/8\right], \tag{A30c}$$
$$\Gamma^y_{xx} = yT\left[3 - y^2\left(10 - r^2\right)/8\right]. \tag{A30d}$$

Appendix B

Polar numerics

Near the poles the grid must be taken to be essentially amorphous. The method we describe here for obtaining accurate numerical operators resembles proposals by *Swarztrauber et al.* [1997] for obtaining differencing coefficients on an icosahedral spherical grid, except we identify the robust stencils without recourse to methods involving singular value decompositions. We rely primarily on the construction of polynomial interpolation schemes, from which each derivative operator is deduced by differentiating the interpolating polynomial. The interpolating polynomial satisfies the "collocation condition", meaning that it exactly fits the given values at the stencil points that specify it. We choose the degree of this polynomial to be greater, by one, than the order of accuracy of the intended gradients. But, for reasons of numerical robustness, we keep the number of stencil points intermediate between the number,

(m+1)(m+2)/2, of independent coefficients of the degree-m interpolating polynomial in x and y and the number, m(m+1)/2, of coefficients of a polynomial of degree one less. For example, for fourth-order gradients, our interpolating polynomial is of degree m=5 and requires 21 coefficients; the stencil of 18 points underspecifies these coefficients but would overspecify the 15 coefficients of a polynomial of only fourth degree.

The additional principle required to make the problem of determining the polynomial coefficients unique is one of parsimony: we require that the m+1 coefficients of terms with maximum degree, i.e. degree m, are kept as "small" as possible (in a sense to be defined below), subject to satisfying the collocation condition.

Let **c'** be the subvector of terms of total degree m taken from the full vector **c** of Taylor coefficients up to and including this degree. Apart from a common scaling factor, there is essentially a unique choice for the quadratic norm ||**c'**|| that remains invariant to rotations of the spatial coordinates x and y. It is this norm we choose to measure the "size" of the terms of highest degree. Defining

$$c'_i = \frac{1}{(m-i)!\,i!}\frac{\partial^m a(\mathbf{x})}{\partial x^{m-i}\partial y^i}, \quad i = 0,\ldots m, \tag{B1}$$

and

$$\| \mathbf{c}' \|^2 = \frac{1}{2}\mathbf{c}'^{\mathrm{T}}\mathbf{N}'\mathbf{c}' \equiv \frac{1}{2}\mathbf{c}^{\mathrm{T}}\mathbf{N}\mathbf{c}\,, \tag{B2}$$

with symmetric kernel **N'**, we obtain **N'** by observing that, if a(**x**) were a realization of a homogeneous random process with a spatially isotropic autocovariance, <a(**x'**),a(**x'**+**x**)>=B(**x**), then the corresponding autocovariance of coefficients **c'** would define the inverse-kernel, $\mathbf{N'}^{-1}$:

$$N'^{-1}_{ij} \propto \left\langle c'_i c'_j \right\rangle = \frac{(-)^m}{i!(m-i)!\,j!(m-j)!}\frac{\partial^{2m} B(\mathbf{x})}{\partial x^k \partial y^{2m-k}} \tag{B3}$$

within a constant of proportionality. But since the terms of degree 2m in the expansion of an isotropic function B(**x**) are those of the summation:

$$\sum_{i=0}^{m} \frac{m!}{i!(m-i)!} x^{2i} y^{2m-2i} \tag{B4}$$

it follows that

$$N^{-1}_{ij} \propto \frac{(k-1)!!(2m-k-1)!!}{i!(m-i)!\,j!(m-j)!} \quad : \quad k \text{ even} \tag{B5a}$$

$$N^{-1}_{ij} \propto 0 \quad : \quad k \text{ odd}, \tag{B5b}$$

where $k = i+j$ and where (k-1)!!=1 . 3… (k-1) for k even.

Centre the coordinates x and y on the target grid point of the stencil of N points $\mathbf{x}_j$ for j=1,…,N and let the elements P_{ij} of matrix $\mathbf{P}$ be the products of powers of the x_j and y_j that combine with expansion coefficients $\mathbf{c}$ to give the truncated Taylor series of function $a(\mathbf{x})$ at this stencil point. Thus, denoting the values of the expansion at the stencil points by the vector $\mathbf{a}$,

$$\mathbf{a} = \mathbf{P}^{\mathrm{T}}\mathbf{c}\,. \tag{B6}$$

The collocation condition requires there to be no distinction between the vector $\mathbf{a}$ interpreted as the given general function $a(\mathbf{x})$ at the stencil points and the vector of values of the reconstructed interpolating polynomial at those points. Introducing a vector $\mathbf{\Lambda}$ of Lagrange multipliers, we find the "smallest" expansion coefficients consistent with collocation by extremizing, with respect to $\mathbf{c}$ and $\mathbf{\Lambda}$, the quantity,

$$\mathcal{L} = \frac{1}{2}\mathbf{c}^{\mathrm{T}}\mathbf{N}\mathbf{c} + \mathbf{\Lambda}^{\mathrm{T}}(\mathbf{P}^{\mathrm{T}}\mathbf{c} - \mathbf{a}) \tag{B7}$$

whose solution, in block matrix form, is:

$$\begin{bmatrix} \mathbf{N} & : & \mathbf{P} \\ \cdots & \cdots & \cdots \\ \mathbf{P}^{\mathrm{T}} & : & \mathbf{0} \end{bmatrix} \begin{bmatrix} \mathbf{c} \\ \cdots \\ \Lambda \end{bmatrix} = \begin{bmatrix} \mathbf{0} \\ \cdots \\ \mathbf{a} \end{bmatrix}. \tag{B8}$$

By inverting the matrix on the left, we may express the result,

$$\mathbf{c} = \mathbf{W}^{\mathrm{T}}\mathbf{a}\,. \tag{B9}$$

Then, for a generic point, $\mathbf{x}$, with powers of x and y arranged in a vector $\mathbf{p}(\mathbf{x})$, like each column of $\mathbf{P}$, we obtain the stencil of interpolation weights as the vector,

$$\mathbf{w}(\mathbf{x}) = \mathbf{W}\mathbf{p}(\mathbf{x})\,, \tag{B10}$$

such that the interpolated estimate of a at generic point $\mathbf{x}$ is given by:

$$\bar{a}(\mathbf{x}) = \mathbf{w}^{\mathrm{T}}(\mathbf{x})\mathbf{a}\,. \tag{B11}$$

The gradient stencils are obtained:

$$\left[\frac{\partial \mathbf{w}}{\partial x}, \quad \frac{\partial \mathbf{w}}{\partial y}\right] \equiv \mathbf{W}\left[\frac{\partial \mathbf{p}}{\partial x}, \quad \frac{\partial \mathbf{p}}{\partial y}\right]. \tag{B12}$$

The combinations of possible stencils with desired number N of points are virtually unlimited. The obvious choice of the nearest set of N points, which works well enough for low-order numerics with small stencils, is often far from optimal at high orders of accuracy. However, it *is* reasonable to expect to find the "best" stencils to comprise only points not very distant from the target. Therefore, we adopt a search algorithm which begins with the nearest N points and progressively examines more dispersed combinations of N neighbouring grid points. To begin, we rank the points by distance from the target grid point, forming the list, n_1, n_2,…etc., in which n_1

designates the target itself. We define a "monotonic sum-L" sequence of N nonnegative integers, d_i, = 1,…,N to satisfy $\Sigma\, d_i = L$ and $d_i \geq d_j$ whenever $i \geq j$. For $N \geq L \geq 0$ the set of such sequences numbers $p(L)$, the number of partitions of L without regard to order, as defined in *Abramowitz and Stegun* [1965, p825], and the individual sequences within the set for a given L can be arranged or generated in lexicographic order. Thus, for L=4 the $p(4)$=5 sequences of size N=6 would be:

(0, 0, 0, 0, 0, 4),
(0, 0, 0, 0, 1, 3),
(0, 0, 0, 0, 2, 2),
(0, 0, 0, 1, 1, 2),
(0, 0, 1, 1, 1, 1).

To each sequence of this type we associate a unique stencil of neighbours, (s_1, s_2, …, s_N), arranged in order of distance from the target, according to:

$$s_k = n_{k+d_k}\,,\ k=1,\ldots,N. \tag{B13}$$

By generating sets of sequences for L = 0, 1, … etc., using the lexicographic ordering defined above, we may systematically examine the possible stencils in a way that enhances the prospect of having located the optimal stencil at any stage of search.

The relative merits of contending stencils are compared using a quadratic norm combining the errors of interpolation of Fourier waves at targets in a small disc centred on the nominal target point of the stencil. These Fourier waves,

$$C(\mathbf{k},\mathbf{x}) = \cos(\mathbf{k}.\mathbf{x}) \tag{B14}$$

$$S(\mathbf{k},\mathbf{x}) = \sin(\mathbf{k}.\mathbf{x}) \tag{B15}$$

produce corresponding errors,

$$\varepsilon_c(\mathbf{k},\mathbf{x}) = \sum_{i=1}^{N} w_i(\mathbf{x}) C(\mathbf{k},\mathbf{x}_i) - C(\mathbf{k},\mathbf{x})\,, \tag{B16}$$

$$\varepsilon_S(\mathbf{k},\mathbf{x}) = \sum_{i=1}^{N} w_i(\mathbf{x}) S(\mathbf{k},\mathbf{x}_i) - S(\mathbf{k},\mathbf{x})\,. \tag{B17}$$

The quantity, $\varepsilon^2(\mathbf{k},\mathbf{x}) = \varepsilon^2{}_C(\mathbf{k},\mathbf{x}) + \varepsilon^2{}_S(\mathbf{k},\mathbf{x})$ is integrated simultaneously over the disc of generic targets, $\mathbf{x}$, surrounding the central stencil point and over a corresponding disc of the resolvable wave vectors $\mathbf{k}$, but weighted by $1/|\mathbf{k}|$ in order to enhance the importance of the larger (smoother) scales. This integral defines the squared error norm we require. These integrations are carried out numerically by sampling the respective discs at uniform intervals of azimuth and using Chebyshev quadrature radially. Adverse stencil configurations can lead to large errors of interpolation at some combinations of target and wave orientation, but the present method ensures that such cases do not go undetected. From a pool typically of several hundred contending stencils, the stencil possessing the smallest error norm is the one chosen for high-order numerical operations.

References

Abramowitz, M., and I.A. Stegun, 1965*: Handbook of mathematical functions*, Dover, New York. 1046pp.

Augenbaum, J. M. and C.S. Peskin, 1985: On the construction of the Voronoi mesh on a sphere. *J. Comput. Phys.*, **14**, 177-192.

Bravais L. & A. Bravais**,** 1837: Essai sur la disposition des feuilles curvisériées. *Ann. Sci. Nat. Bot. Biol. Vég.*, 7: 42-110, 193-221, 291-348; 8: 11-42.

Chukkapalli, G., S.R. Karpik and C.R. Ethier, 1999: A scheme for generating unstructured grids on spheres with application to parallel computation. *J. Comp. Phys*., **149**, 114-127.

Chynoweth, S. and M.J. Sewell, 1990: Mesh duality and Legendre duality. *Proc R. Soc. Lond*., **A 428**, 351-377.

Conway, J.H. and R.K. Guy, 1996: *The book of numbers*, Copernicus, New York. 310pp.

Cullen, M.J.P., 1974: Integrations of the primitive equations on a sphere using the finite-element method. *Q. J. Roy. Meteorol. Soc*., **114**, 1321-1346.

Douady, S. and Y. Couder, 1992: Phyllotaxis as a physical self-organized growth process. *Physical Rev. Lett*., **68**, 2098-2101

Gates, W.L. and C.L. Riegel, 1962: A study of numerical errors in the integration of barotropic flows on a spherical grid. *J. Geophys. Res*., **67**, 773,784.

Hannay, J.H. and J.F. Nye, 2004: Fibonacci numerical integration on a sphere. *J. Phys. A: Math. Gen.*, **37**, 11591-11601.

Hoskins, B.J., 1973: Stability of the Rossby-Haurwitz wave. *Q. J. Roy. Meteorol. Soc*., **99**, 723-745.

Kageyama, A., and T. Sato, 2004: "Yin-Yang grid": An overset grid in spherical geometry. *Geochemistry, Geophysics, Geosystems*, **5**, Art. No. Q09005.

Kurihara, Y., 1965: Numerical integration of the primitive equations on a spherical grid. *Mon. Wea. Rev*., **93**, 399-415.

Majewski, D., D. Liermann, P. Prohl, B. Ritter, M. Buchhold, T. Hanisch, G. Paul, W. Wergen and J. Baumgardner, 2002: The operational global icosahedral-hexagonal gridpoint model GME: Description and high-resolution tests, *Mon. Wea. Rev.*, **130**, 319-338.

Michalakes, J.G., R.J. Purser and R. Swinbank, 1999: Data structure and parallel decomposition considerations on a Fibonacci grid. *Preprints of the 13th conference on Numerical Weather Prediction*, (Denver, 13-17 September 1999), American Meteorological Society, 129-130.

Pearson, F., II: 1990: *Map projections*. CRC, Baton Rouge. 372pp.

Press, W.H., S.A. Teukolsky, W.T. Vetterling and B.P. Flannery, 1996: *Numerical recipes in Fortran 77: The art of scientific computing*, Cambridge University Press. 933pp.

Purser, R.J., 1999: Non-standard Grids. ECMWF seminar on "Recent Developments in Numerical Methods for Atmospheric Modelling" 7-11 Sep. 1998, 44-72.

Purser R.J., and R. Swinbank, 2006: Generalized Euler-Maclaurin formulae and end corrections for accurate quadrature on Fibonacci grids. NOAA/NCEP Office Note (submitted).

Rančić, M., R.J. Purser and F. Mesinger, 1996: A global shallow-water model using an expanded spherical cube: gnomonic versus conformal coordinates. *Q. J. Roy. Meteorol. Soc*., **122**, 959-982.

Ronchi, C., R. Iacano and P.S. Paolucci, 1996: The 'cubed sphere': a new method for the solution of partial differential equations in spherical geometry. *J. Comp. Phys.*, **124**, 93-114.

Sadourny, R., 1972: Conservative finite-differencing approximations of the primitive equations a quasi-uniform spherical grids. *Mon. Wea. Rev.*, **100**, 136-144

Sadourny, R., A. Arakawa and Y. Mintz, 1968: Integration of the non-divergent barotropic vorticity equation with an icosahedral-hexagonal grid for the sphere. *Mon. Wea. Rev*., **121**, 351-356.

Saff, E.B. and A.B.J. Kuijlaars, 1997: Distributing Many Points on a Sphere. *The Mathematical Intelligencer*, **19**, 5-11.

Salmon, R., 1983: Practical use of Hamilton's principle. *J. Fluid Mech.*, **132**, 431-444

Salmon,R., 1985: New equations for nearly geostrophic flow. *J. Fluid Mech.*, **153**, 461-477.

Stewart, I., 1998: Flowers for Fibonacci. *Life's other secret*, John Wiley, 121-136.

Swarztrauber, P.N., D.L. Williamson and J.B. Drake, 1997: The cartesian method for solving partial differential equations in spherical geometry. *Dyn. Atmos. Ocean*., **27**, 679-706.

Swinbank, R. and R.J. Purser, 1999: Fibonacci Grids. *Preprints of the 13th conference on Numerical Weather Prediction*, (Denver, 13-17 September 1999), American Meteorological Society, 125-128.

Synge, J. L., and Schild, 1978: *Tensor Calculus*. Dover, NY.

Takahashi, K., X. Peng, K. Komine, M. Ohdaira, Y. Abe, T. Sugimura, K. Goto,H. Fichigami, and M. Yamada, 2005: Non-hydrostatic atmospheric GCM development

and its computational performance. ECMWF Workshop on High Performance Computing in Meteorology, 25-29 October 2004 (in press).

Thuburn, J., 1997: A PV-based shallow-water model on a hexagonal-icosahedral grid. *Mon. Wea. Rev*., **125**, 2328-2347.

Thuburn, J. and Y. Li, 2000: Numerical simulations of Rossby-Haurwitz waves. *Tellus A*, 52, 181-189.

Vogel, H., 1979: A better way to construct the sunflower head. *Mathematical Biosciences*, **44**, 179-189

Williamson, D.L., 1968: Integration of the barotropic vorticity equation on a spherical geodesic grid. *Tellus*, **20**, 642-653.

Williamson, D.L, J.B. Drake, J.J. Hack, R. Jakob and P.N. Swarztrauber, 1992: A standard test set for numerical approximations to the shallow water equations in spherical geometry. *J. Comp. Phys*., **102**, 211-224.

Figure Captions

Figure 1: A planar "Fibonacci Grid", in which a disk is covered uniformly with 700 points. Every 34^{th} and 55^{th} point is marked with an open circle, to highlight the spiral structure of the grid.

Figure 2: A spherical Fibonacci grid, at resolution N=1000 (2001 grid points). As in Fig. 1, the spiral structure is highlighted by marking every 34^{th} and 55^{th} grid point.

Figure 3: Arrangement of Fibonacci grid points on a cartesian coordinate system, with the x-coordinate representing λ and the y-coordinate $\sin\theta$. This shows how a set of basis vectors is constructed, based on the spiral grid structure. The components of the basis vectors can be written in terms of the circumference C and the y-interval between successive grid-points, δ.

Figure 4: The a) Delaunay triangulation and b) Voronoi mesh for the grid points illustrated in Fig. 2.

Figure 5: Histograms of the areas of the Voronoi cells at a) N=1000, as shown in Fig. 4, b) N=10000 and c) N=100000. The x-coordinate shows the area, as a ratio to the average value and the y-coordinate shows the number of cells with area more extreme than the given value. The y-axis is truncated for the higher resolutions, where most areas are very close to the average.

Figure 6: An example of a variable-resolution Fibonacci grid (N=1000), in which the density of points is three times greater at the equator than at high latitudes.

Figure 7: Results of polar advection test at a) N=5000 and low diffusion, b) N=5000, c) N=20000. The dashed lines show the initial location of the cosine bell, and the full lines the final location, which should coincide exactly.

Figure 8: Statistical comparisons between polar advection test results and the true solution. Statistics L_1, L_2 and L_∞ are plotted daily from day 0 to day 12, through a complete revolution.

Figure 9: Height fields from simulations of the Rossby-Haurwitz wave: a) initial conditions, day0; b) day14 from the reference solution; c) day14, simulation using N=5000; d) day 14, simulation using N=20000.

Figure 10: Statistics L_1, L_2 and L_∞ for Rossby-Haurwitz wave simulations at resolution N=5000 and N=20000, compared with the reference solution

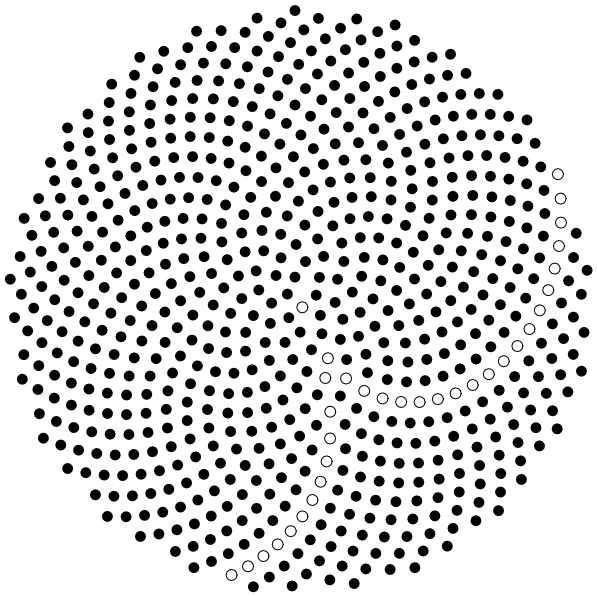

Figure 1: A planar "Fibonacci Grid", in which a disk is covered uniformly with 700 points. Every 34^{th} and 55^{th} point is marked with an open circle, to highlight the spiral structure of the grid.

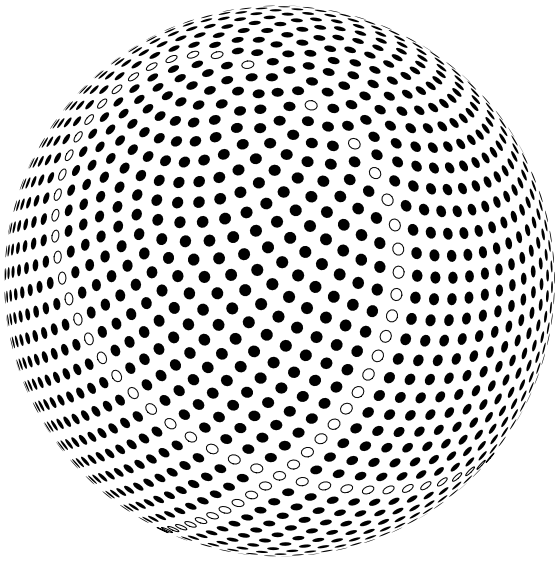

Figure 2: A spherical Fibonacci grid, at resolution N=1000 (2001 grid points). As in Fig. 1, the spiral structure is highlighted by marking every 34^{th} and 55^{th} grid point.

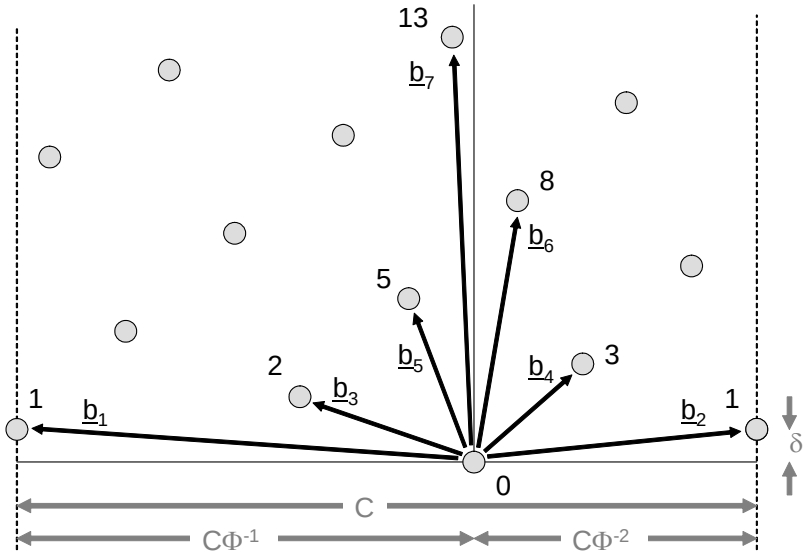

Figure 3: Arrangement of Fibonacci grid points on a cartesian coordinate system, with the x-coordinate representing λ and the y-coordinate $\sin\theta$. This shows how a set of basis vectors is constructed, based on the spiral grid structure. The components of the basis vectors can be written in terms of the circumference C and the y-interval between successive grid-points, δ.

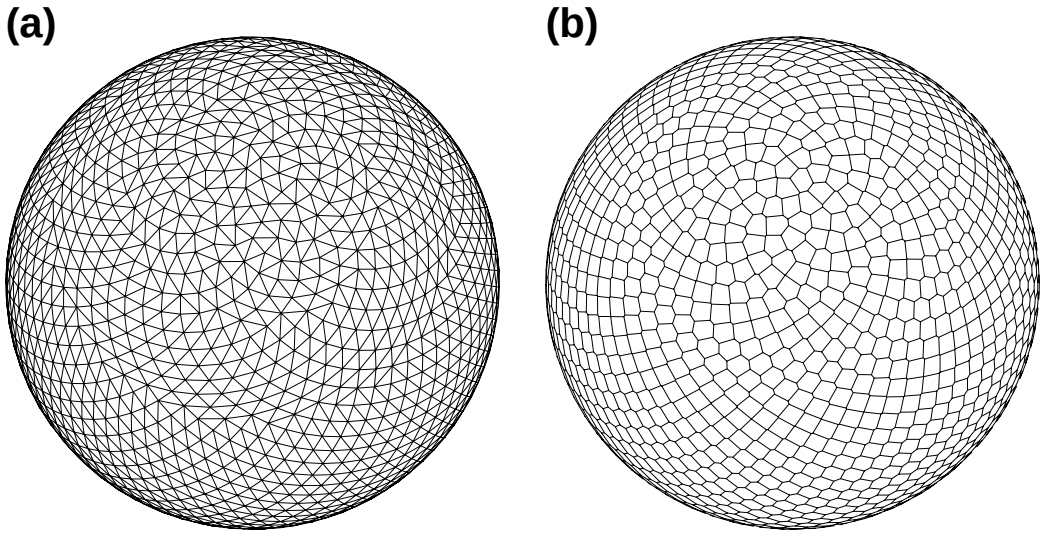

Figure 4: The a) Delaunay triangulation and b) Voronoi mesh for the grid points illustrated in Fig. 2.

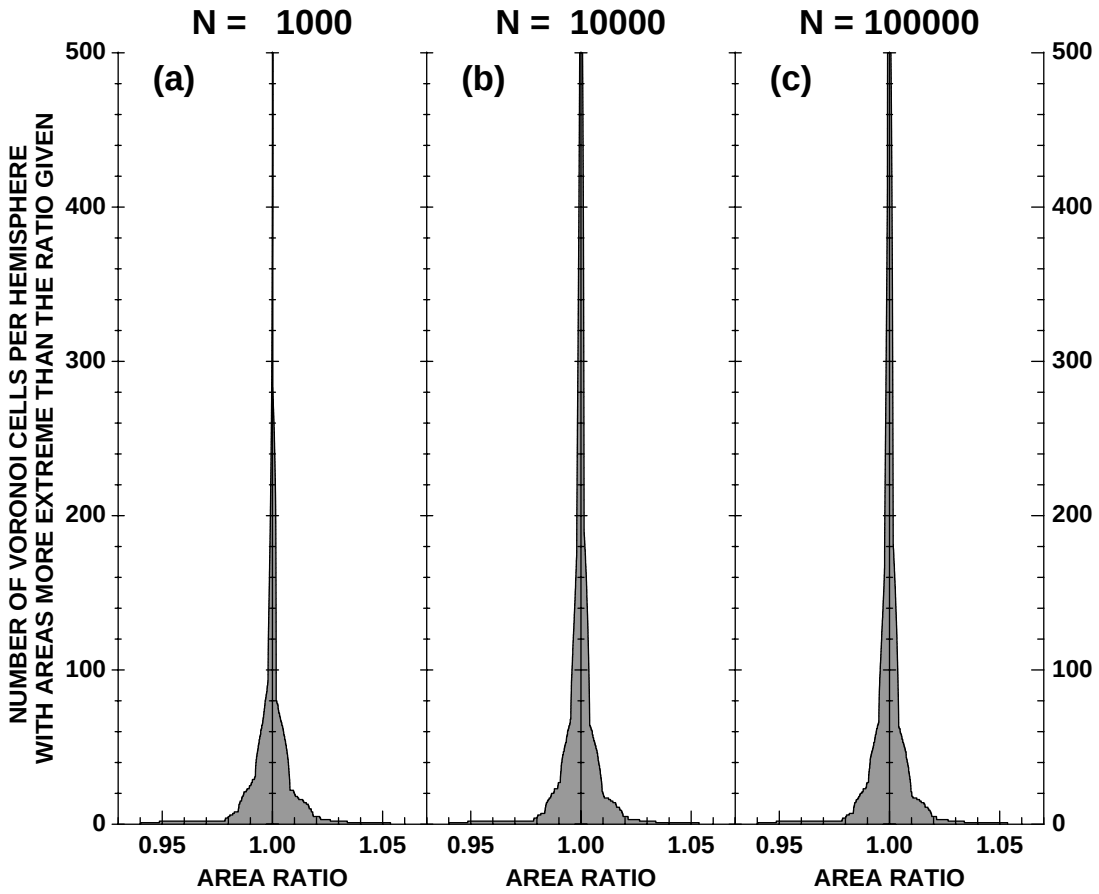

Figure 5: Histograms of the areas of the Voronoi cells at a) N=1000, as shown in Fig. 4, b) N=10000 and c) N=100000. The x-coordinate shows the area, as a ratio to the average value and the y-coordinate shows the number of cells with area more extreme than the given value. The y-axis is truncated for the higher resolutions, where most areas are very close to the average.

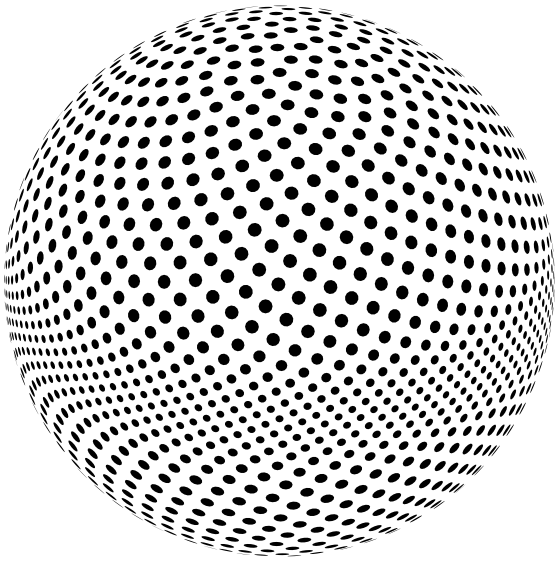

Figure 6: An example of a variable-resolution Fibonacci grid (N=1000), in which the density of points is three times greater at the equator than at high latitudes.

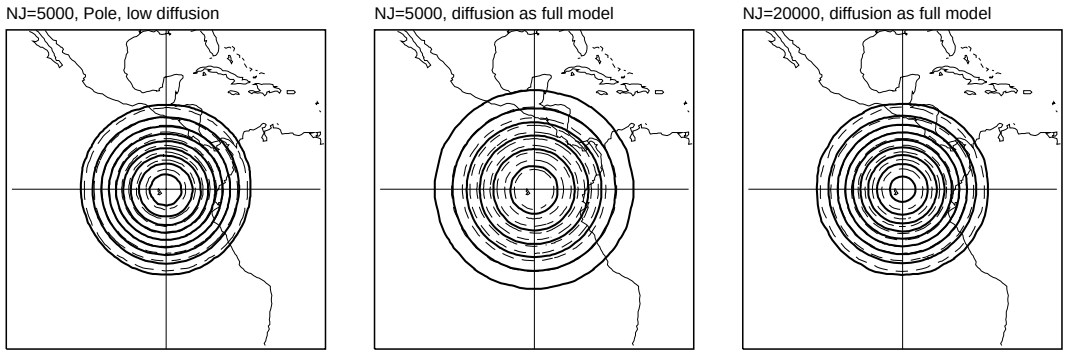

Figure 7: Results of polar advection test at a) N=5000 and low diffusion, b) N=5000, c) N=20000. The dashed lines show the initial location of the cosine bell, and the full lines the final location, which should coincide exactly.

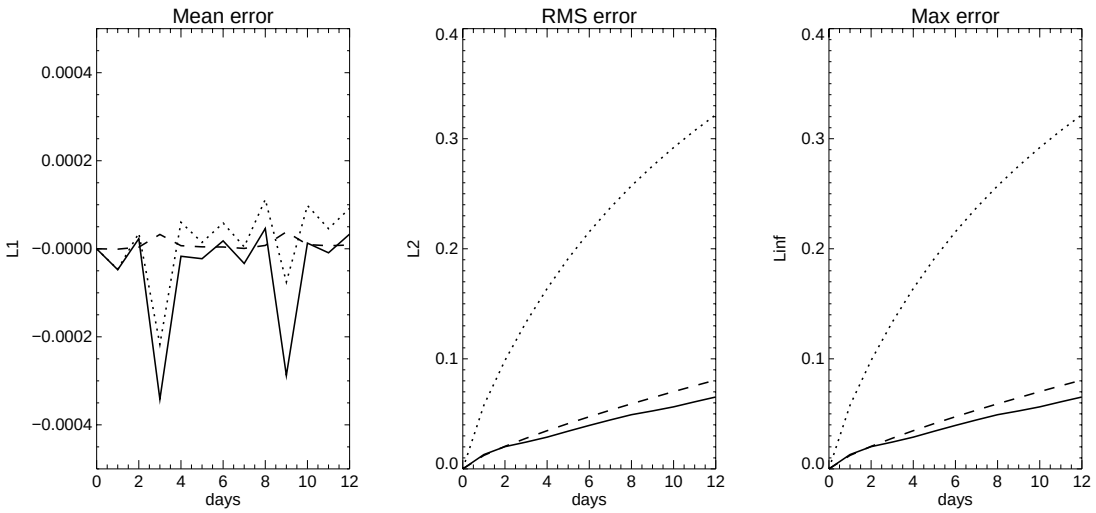

Figure 8: Statistical comparisons between polar advection test results and the true solution. Statistics L_1, L_2 and L_∞ are plotted daily from day 0 to day 12, through a complete revolution. Solid line – N=5000, low diffusion; dotted line – N=5000, with diffusion as in full model; dashed line – N=20000, with diffusion as in full model.

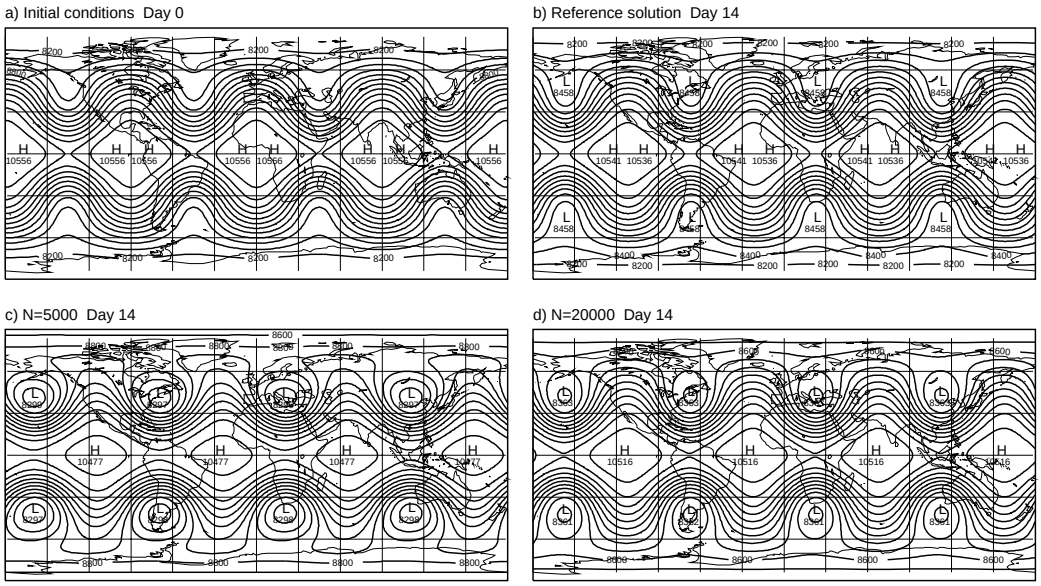

Figure 9: Height fields from simulations of the Rossby-Haurwitz wave: a) initial conditions, day0; b) day14 from the reference solution; c) day14, simulation using N=5000; d) day 14, simulation using N=20000.

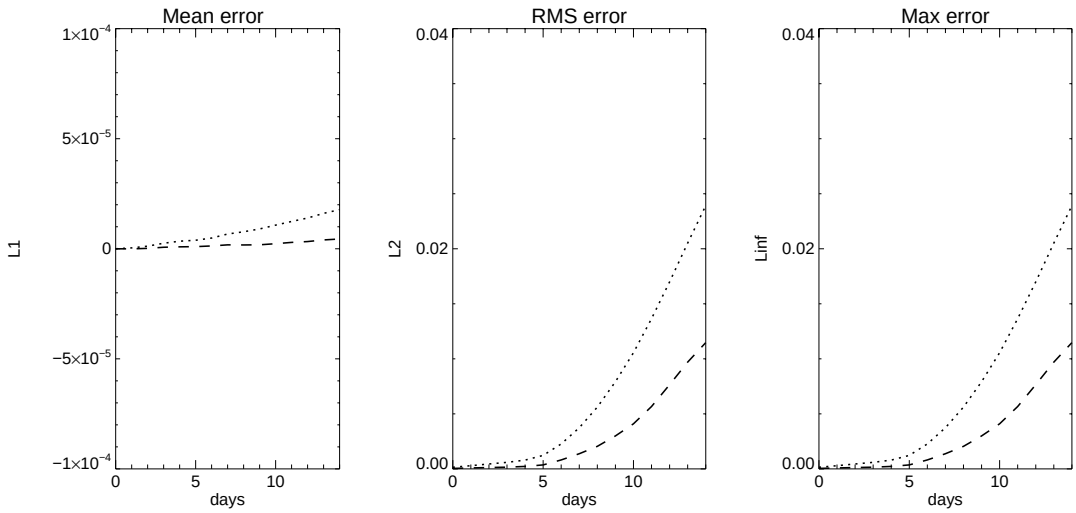

Figure 10: Statistics L_1, L_2 and L_∞ for Rossby-Haurwitz wave simulations at resolution N=5000 (dotted line) and N=20000 (dashed line), compared with the reference solution